ADVANCED MATERIALS
www.advmat.de

Directional Acoustic Antennas Based on Valley-Hall Topological Insulators

Zhiwang Zhang, Ye Tian, Yihe Wang, Shuxiang Gao, Ying Cheng, Xiaojun Liu,* and Johan Christensen**

Realizing directional acoustic signal transmittance and reception robust against surrounding noise and competing signals is crucial in many areas such as communication, navigation, and detection for medical and industrial purposes. The fundamentally wide-angled radiation pattern of most current acoustic sensors and transducers displays a major limitation of the performance when it comes to precise targeting and probing of sound particular of interest in human speaking and hearing. Here, it is shown how topological acoustic valley transport can be designed to enable a unique beamforming mechanism that renders a superdirective needle-like sound radiation and reception pattern. The strategy rests on out-coupling valley-polarized edge states, whose beam is experimentally detected in the far-field with 10° width and a sound-intensity enhancement factor ≈10. Furthermore, anti-interference communication is proposed where sound is received from desired directions, but background noise from other directions is successfully suppressed. This type of topological acoustic antenna offers new ways to control sound with improved performance and functionalities that are highly desirable for versatile applications.

Aquatic animals like dolphins can produce directional acoustic wave beams of about 16° in width for detecting and tracking prey with high resolution in a blind and noisy environment. This unique function of the dolphins' acoustic communication system is based on an acoustic lens, which acts as a sophisticated biosonar. Fatty acoustic tissue with a specific configuration of the mass density in the dolphin melon and lower jaw serve the purpose of a lens, which both helps the dolphin to direct sound into the environment and to detect the echoes that return upon reflections. Unlike dolphins, the function of human's acoustic communication system is given by the conventional outer ear and mouth structures, which are based on the acoustic horn concept rather than an acoustic lens, thus bringing forth sound emission/reception of poor directivity to/from almost every direction.[1–3] To overcome this disadvantage, parametric loudspeaker and microphone array systems based on phased-array technology have been developed to achieve beamforming relying upon a very large transducer array with a complex signal processing system to obtain reasonable spatial resolutions.[4] Recently, some pioneering devices based on phononic crystals (PnCs)[5] and locally-resonant metamaterials[6] have been demonstrated to achieve directional sound emission or reception.[7–10] However, the specific flat equifrequency contour of PnCs and the resonant characteristic in metamaterials structure fundamentally limit the achievable beamwidth and working frequency range. In addition, duplex-devices both with the ability of emitting and receiving signals remain a great challenge in both physics and engineering. Therefore, there is a great need to develop a novel scheme and functional devices for superdirectional duplex acoustic communication that can overcome the limitations of current acoustic technologies.

On the other hand, "topological acoustics" has attracted considerable attention over the past two years due to the fascinating quantum-like effects in acoustic systems,[11–33] which originates from studies of condensed-matter states.[34,35] Earlier pioneering approaches in the quest for constructing acoustic topological states in 2D systems relied on circulating fluid flows to mimic the quantum Hall effect,[11,14,15] coupled resonator ring waveguides to mimic Floquet topological insulators,[16,19,20,23] phononic "graphene" with double Dirac cones to mimic the quantum spin Hall effect[17,18,22,27–29] and C_{3v} point symmetry phononic crystals composed of triangular rods,[24,31,33] square lattices containing square inclusions[30] to design a new class of valley-Hall topological insulators (VHTI).[36–38] Furthermore, recently extensions into 3D were launched demonstrating the existence of Weyl points and Fermi arcs in topological acoustics.[13,21,32]

Here, we extend the concept of topological order to acoustic communication, and report a superdirectional topological

Dr. Z. Zhang, Dr. Y. Tian, Dr. Y. Wang, Dr. S. Gao, Prof. Y. Cheng, Prof. X. Liu
Department of Physics
MOE Key Laboratory of Modern Acoustics
Collaborative Innovation Center of Advanced Microstructures
Nanjing University
Nanjing 210093, China
E-mail: chengying@nju.edu.cn; liuxiaojun@nju.edu.cn
Prof. J. Christensen
Department of Physics
Universidad Carlos III de Madrid
ES-28916 Leganés, Madrid, Spain
E-mail: johan.christensen@uc3m.es

DOI: 10.1002/adma.201803229

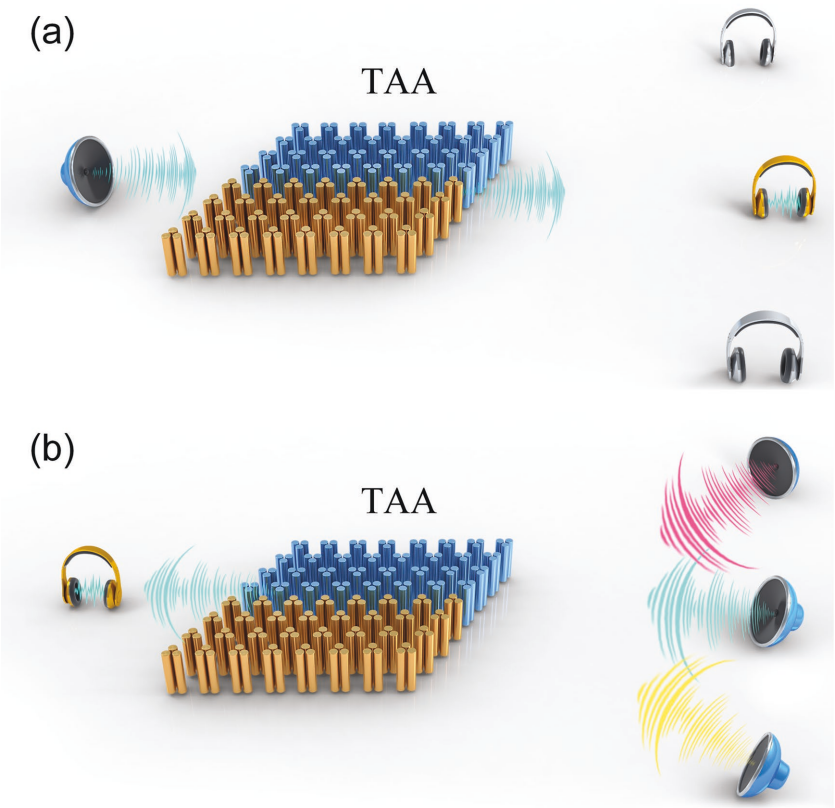

Figure 1. Schematic and function of the topological acoustic antenna (TAA). a) Superdirectional sound focusing targeted at the right audience (cyan) without disclosing information to unwanted listeners. b) Superdirectional sound reception to detect sound from a desired source while noise is suppressed coming from other directions. The TAA is insonified from various sources (red/cyan/yellow) that interfere with each other but receives only the signal from a predefined direction (cyan).

acoustic antenna (TAA) for audible sound based on VHTIs (see **Figure 1**). These topological insulators allow helical sound propagation (i.e., with right- or left-hand circular polarization labeled as RCP and LCP) within each K or K′ valley of the band structure, in which the angular rotation of the acoustic wave function generates an intrinsic angular momentum analogous to that produced by the electron spin. This behavior enables topological valley transport at the interface between such two VHTIs of different symmetry-broken geometries. Moreover, we demonstrate that the helical edge states hosted by the topological antenna can both be excited or out-coupled in a highly directional fashion, thus providing sophisticated acoustic duplex communication. In that sense, we measure how the TAA emits very narrow output beams useful for focusing sound targeted at a specific audience without disclosing information to undesired listeners (Figure 1a) and also how sound can be perfectly received in the presence of interfering white noise, e.g., unwanted traffic noise (Figure 1b). To some extent, we demonstrate the topological version of a dolphin's biosonar, but more importantly, we suggest how topological acoustics can improve anti-interference and high signal-to-noise communications.

In time-reversal invariant systems, breaking the mirror symmetry provides an opportunity to obtain topological modes transitions and to launch edge states. We start from the acoustic Kagome lattice PnC,[26] in which the C_3 spatial symmetry is at the origin of the topological order where a reduction of the C_6 symmetry through manipulating the hopping amplitudes κ and γ induces the topological phase transition. As shown schematically in **Figure 2**a, we employ isotropic rigid rods to construct the Kagome lattice where $a = 2.17$ cm, the rod radius $r = 0.30$ cm, and the distance between the center of rod and the center of unit cell is $d = \sqrt{3}a/6$. We introduce lattice deformation to break the C_6 symmetry and select two inverted topological phases. When shrinking the distance d_1 to 0.40 cm, the triangular lattice hosts erected trimers as seen in the inset of Figure 2b. On the contrary, when the distance is expanded to $d_2 = 2d - d_1 = 0.85$ cm, the lattice can be treated as the triangular lattice of upside-down trimers (inset of Figure 2c). To illustrate the modes inversion process accompanied by the broken symmetry, the corresponding dispersion relations are shown in Figure 2b,c, respectively. It is predicted that both dispersion relations of the PnCs display a pair of well-defined extrema (i.e., valley states) at the corners of the 1st Brillouin zone (BZ), which are separated by an omnidirectional band gap from 8.262 to 9.312 kHz. For simplicity, we focus on the topological properties of the valley states at the K point, and those for the inequivalent K′ point can be deduced directly from the time-reversal symmetry. The distribution of the absolute pressure fields and intensities of the valley pseudospin states are illustrated in the insets of Figure 2b,c. These acoustic valley pseudospin states exhibit opposite chirality analogous to the electronic valley states. When the trimers are erected in the triangular lattice, the acoustic vortex is clockwise-polarized (LCP) and labeled as K_- at the lower state and counterclockwise-polarized (RCP) and labeled as K_+ at the higher state. For the upside-down case, this scenario is opposite leading to an inverted band structure. The dynamic intensity vortex around the trimer center at the K valley is shown in Movie S1 of the Supporting Information. We emphasize that the closing and reopening process of the Dirac cone is realized by simply rotating the acoustic trimers (Note S1, Supporting Information).

Launching of and coupling to valley-polarized edge states is the key mechanism behind the highly directional TAA. We demonstrate that the interface between two valley-Hall PnCs containing different valley polarizations sustains localized edge states that are excluded from the bulk. **Figure 3**a illustrates dispersion relations of the ribbon-shaped supercell composed of 20 erected trimers and 20 upside-down trimers separated by a zigzag interface, as shown in the inset of Figure 3a. The zigzag interface can be engineered in two distinct ways, which, according to the resulting refraction angle of the emitted beams, are labeled as a positive/negative-type interface. The emergence of the helical edge states in the bulk band gap are depicted by the red dashed line for the negative-type interface and the blue

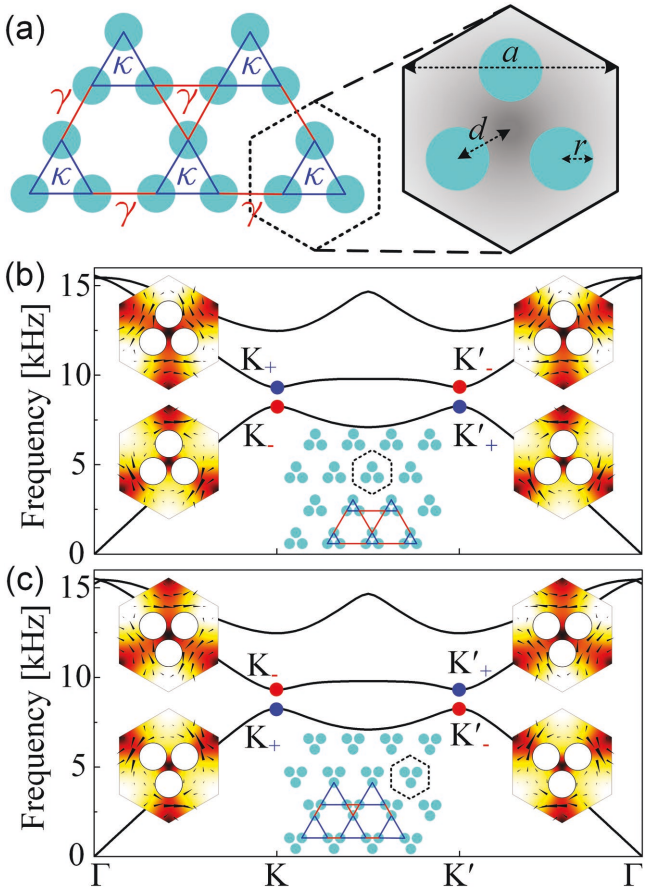

Figure 2. Acoustic valley pseudospin states and topological modes inversion. a) Schematic cross-section of a 2D Kagome lattice in an air matrix. Inset: the unit cell. b,c) Dispersion relations of the acoustic modes in a triangular lattice composed of the shrunk/expanded acoustic trimers. K_+, K_-, K'_+ and K'_- denote the different valley pseudospin states. The color legend represents the amplitude of absolute pressure of the valley states. The black arrows indicate the direction and amplitude of the intensity (see Movie S1 of the Supporting Information for dynamic view of the pseudospin states).

solid line for the positive-type interface, each having opposite group velocities. The edge states originate from the change of valley-Chern index across the interface between topologically distinct regions. The nonvanishing valley-Chern indices can be determined by $2C^{(K',K)} = \pm 1 \times \mathrm{sgn}(\Delta_P)$.[24,39–41] Here, Δ_P characterizes the geometrical perturbation where the sign determines the orientation of the acoustic trimer (Note S2, Supporting Information). Specifically, $\Delta_P < 0$ ($\Delta_P > 0$) for the shrunk (expanded) Kagome lattice, that is, the VHTI of erected (upside-down) trimers. Hence, for the negative-type interface, there should be a backward-moving edge state at K′ point due to $\Delta C^{(K')} = C^{(K')}_{\mathrm{upper}} - C^{(K')}_{\mathrm{lower}} = -1$, and a forward-moving edge state at K point with $\Delta C^{(K)} = 1$. Note that for a given valley, there is only one edge mode propagating along the direction that is locked to that valley.

In order to verify the topologically protected edge states, we fabricate a finite VHTI containing $30a \times 30a$ unit cells whose interface separating the two PnCs is insonified normally by a continuous sinusoidal sound wave, see Figure 3b. For

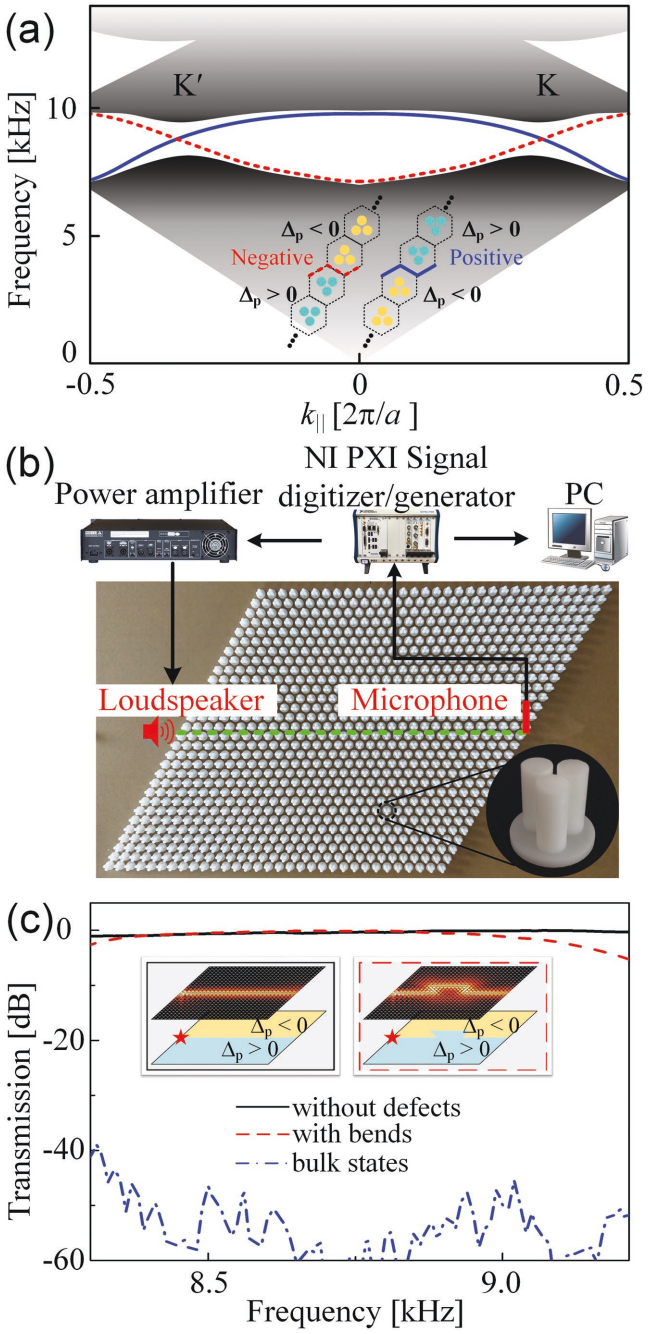

Figure 3. Topologically protected edge waves localized at the interface of PnCs with different valley polarizations. a) Dispersion relation of the ribbon-shaped 2D PnC containing different interfaces. Dark gray regions represent the bulk modes and the dashed red/solid blue lines represent the negative-type/positive-type interfaces as shown in inset. b) Photograph of the fabricated VHTI (without the top cover). c) Measured transmission spectra of the topological valley transport with/without bends. Inset: simulated absolute pressure fields at the frequency $f = 9.20$ kHz.

conventional PnCs composed alone of erected trimers, the bulk states cease to exist in the topological band gap leading to a measured transmission below –40 dB (blue dashed-dotted line in Figure 3c). However, when sound waves are localized in the proximity of the straight or bended interface in the form

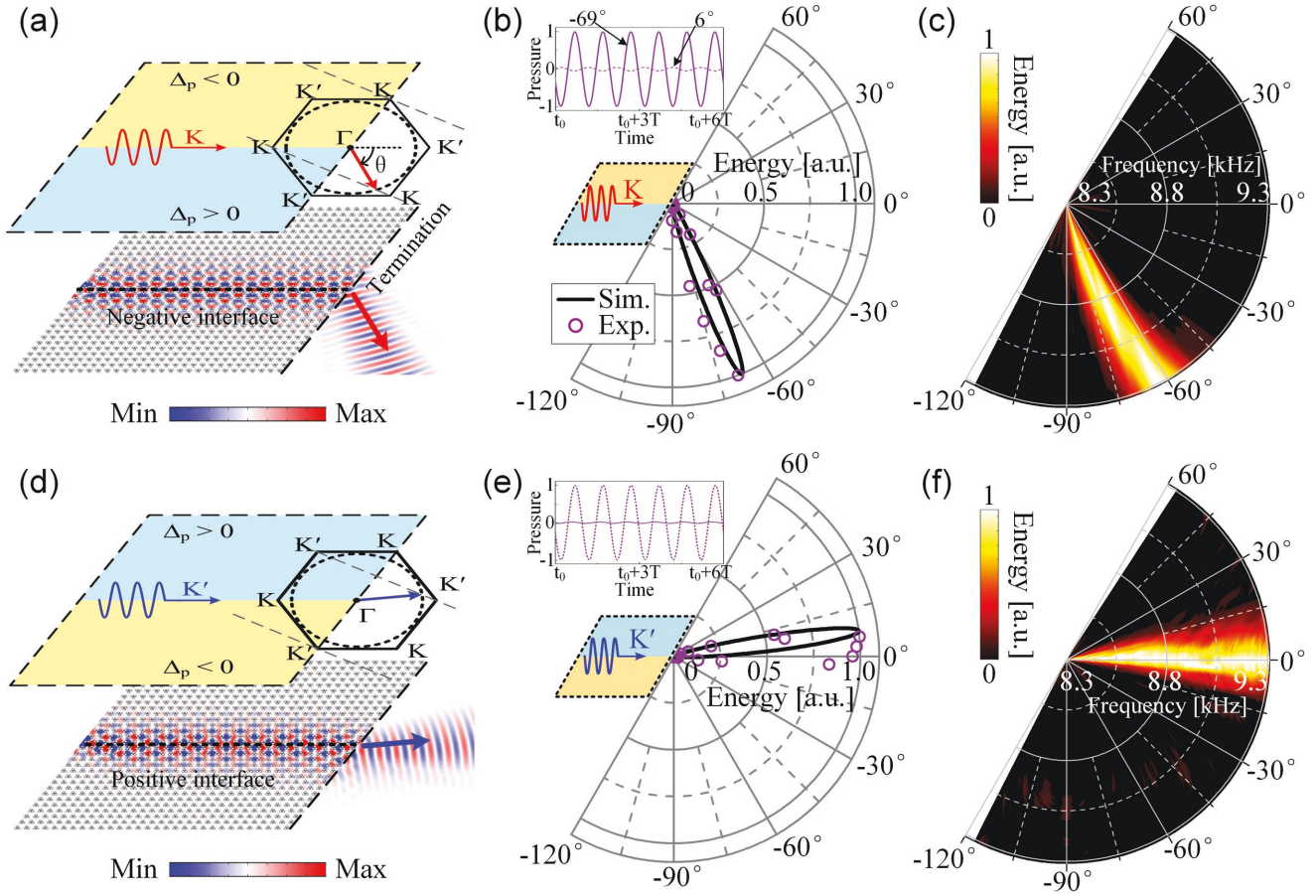

Figure 4. Superdirectional sound radiation by out-coupling of valley-polarized edge states from the TAA. a) *k*-space analysis on the out-coupling of K projected edge states along the negative-type (zigzag) interface. Black solid hexagon represents the 1st BZ and the black dashed circle shows the dispersion in air. Bottom panel: the simulated distribution of pressure fields at the frequency $f = 8.66$ kHz. b) Simulated and measured far-field pattern with normalized energy emerging the negative-type interface at $f = 8.66$ kHz. Inset: pressure signals in the time-domain measured at −69° and 6°. $T = 1/f$ is the time period of sound wave. c) Experimentally detected spectral relation between the acoustical energy and the directional angle within the entire topological band gap. d–f) Corresponding analysis on the out-coupling of K′ projected edge state along the positive-type (zigzag) interface.

of valley polarized edge states, high transmissions within the entire topological band gap are sustained, confirming the remarkable immunity of topological valley transport as seen in Figure 3c.

The valley-polarized edge states observed above originate inherently from valley-projection, which guarantees reflection-free out-coupling from the topological interface into the free-space[41] (see Note S3 of the Supporting Information for comparisons to an ordinary waveguide). We begin by demonstrating the directional emission into free-space of out-coupled edge states along both positive- and negative-type interfaces in TAAs. The suppression of inter-valley scattering depends on the types of termination of the sample. The antenna terminals are cut along the zigzag direction, which produces a vanishing intervalley field overlap unlike an armchair-type termination that produces significant unwanted diffraction.[41] As shown in **Figure 4**, the direction of the outgoing beam into air depends on the type of valley (K or K′) from which the edge state is projected. Hence, sound waves that are launched from left to right along the negative-type interface are projected from the K valley (Figure 4a), and conversely along the positive-type interface are projected from the K′ valley (Figure 4d). To illustrate the refraction of the radiated beam, we draw the equifrequency curves in free-space (black dashed circle in Figure 4a,d) and the BZ (black solid regular hexagon in Figure 4a,d) on a scale that represents the relative magnitudes of the wavevectors of the incident and refracted waves. By matching the parallel component of the incident wavevector $\boldsymbol{K}$ on to the equifrequency curve of free-space, one is able to find the propagation direction of the radiated beam. The theoretical refraction angle $\theta^{-}_{\text{theory}}$ (for the negative-type interface) can be quantitatively determined by the phase-matching condition $\boldsymbol{k} \cdot \boldsymbol{e}_{\text{term}} = \boldsymbol{K} \cdot \boldsymbol{e}_{\text{term}}$, which is $|\boldsymbol{k}| \cdot \cos(120° + \theta^{-}_{\text{theory}}) = |\boldsymbol{K}| \cdot \cos 60°$, ultimately giving rise to a refraction angle of $\theta^{-}_{\text{theory}} = -67.47°$ at the frequency $f = 8.66$ kHz (Note S4, Supporting Information). Likewise, at the same frequency, analytically we calculate the refraction angle for the positive-type interface TAA shown in Figure 4d to be $\theta^{+}_{\text{theory}} = 7.47°$. In order to verify this analysis, we scanned the far-field radiation pattern within an angular range as shown in Figure 4, both by means of numerical simulations and measurements. We obtain, for the TAA having the negative-type interface, refraction angles as predicted $\theta^{-}_{\text{sim}} = -67.86°$ and measured $\theta^{-}_{\text{exp}} = -69°$

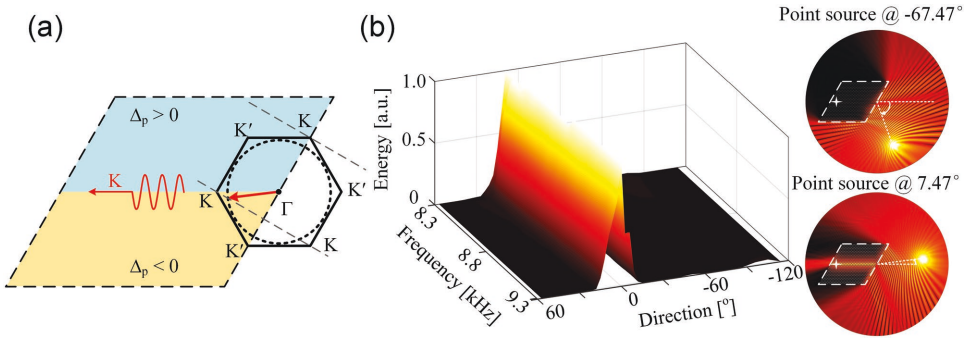

Figure 5. Superdirectional sound reception through excited valley-polarized edge states. a) *k*-space analysis of externally excited K projected edge states along the positive-type interface. b) Experimentally measured acoustic energy in dependence of the angle of the point source with respect to the interface and frequency within the topological band gap. Insets: Simulated distributions of absolute pressure fields with the point source placed at –67.47° and 7.47°, respectively. The frequency $f = 8.66$ kHz. Sound energy is measured at the far-side terminals of the TAA, which is labeled by a white star shown in insets of (b).

as seen in Figure 4b. Note that the working frequencies of the TAA span across the entire frequency range of the topological band gap (see Note S5, Supporting Information). With the positive-type interface we obtain: $\theta^{+}_{sim} = 7.74°$ and $\theta^{+}_{exp} = 6°$, shown in Figure 4e. Additionally, as shown in the insets of these figures, we measure the pressure signals in the time-domain, in each case, both refraction angles $\theta^{+/-}_{exp}$ are considered, –69° and 6°. These results show that the superdirectional out-coupled edge states indeed obey the valley-projected selection rule with time, such that the TAA with the negative (positive)-type interface suppresses sound refraction with positive (negative) angles. Three remarks are made: (1) The experimental results are in good agreement with the simulated ones, however, the minor angular differences measured should be ascribed to the 3° intervals between adjacent detecting positions (Experimental Section). (2) The half-power beamwidth of the main lobe is measured to be 9.72° (9.54°) for the TAA with the negative (positive)-type interface, whereas the side lobes have been completely eliminated in agreement with a pronounced beam efficiency of 97.51% (Note S6, Supporting Information). Hence, the collimated out-coupling of valley-polarized edge states thus provides a very useful means in focusing sound toward a targeted audience only. (3) We further compare the efficiency with a conventional point source radiating sound waves omnidirectionally with a far-field peak amplitude 10.3 times less than the TAA. This finding confirms that superdirectional radiation in the far-field prevails at reasonably large sound levels (Note S7, Supporting Information). Lastly, as illustrated in Figure 4c,f through the experimentally observed far-field energy spectra, we emphasize that the proposed acoustic antenna functions in the entire topological band gap spanning between 8.30 and 9.31 kHz. Conclusively, designing the acoustic antenna based on topological valley transport, ensures protected and efficient energy transmission, which is only marginally affected by size variations and perturbations within the TAA and its terminal (Notes S8–S10, Supporting Information) provided that no air gap separates the TAA (Note S11, Supporting Information).

In reverse, through the coupling to localized edge states along the positive-type interface, we utilize the TAA to receive sound from a radiating point source in a highly collimated fashion. When the wavevector of incoming sound in free space satisfies the phase-matching condition to a specific valley, the corresponding projected edge mode can be excited, which result in the acoustic signal detection of the TAA as illustrated in **Figure 5**a. For example, as illustrated in Figure 5, edge states that are flanked by the positive-type interface produce a superdirectional beam on the antenna far-side terminal. The point source emitting sound at 8.66 kHz and placed at 7.47° with respect to the interface is able to excite this state as projected by the K valley (directional sound reception by the TAA with a negative-type interface is discussed in Note S12, Supporting Information). Other point sources placed away from 7.47° are not allowed to enter the TAA via its interface. In the top inset of Figure 5b the scenario is simulated where a point source is placed at –67.47°, depicting zero energy reception. To make a global picture of the selectiveness of the topological antenna, we measured the reception of an emitting point source at frequencies within the range of the topological band gap. Additionally, at a 3° interval and a constant distance of 0.65 m from the TAA near-side interface, the signal source was angularly displaced from –120° to 60°. The measured results shown in Figure 5b indeed depict the highly directive response of the TAA. The received output power that is normalized to the maximum value displays a spectrally constant profile, which is spatially locked at 6° and showing very little variation with frequency. This spectrally insensitive antenna character is indispensable for filtering in broadband signal environments in which the desired source and the competing signals cover approximately the same bandwidth. Furthermore, the proposed TAA has been also tested to accurately locate an individual source within a practical acoustic environment such as a reverberation chamber, which gives rise to highly unwanted interference echoes (see Note S13, Supporting Information).

The ability in acoustic communication not only to improve the speech understanding of the listeners efficiently in the presence of background noise, but also to pick up sound from a targeted source is highly desired in many areas. We demonstrate that the excitation of valley-polarized edge states flanked by a positive-type interfaced TAA and the reception of signals remain highly efficient despite being subject to a noisy acoustic environment. In a typical acoustic environment, the interfering sources generally originate from points in space separated from the actual sound source of interest. As illustrated in **Figure 6**a, the intent is to mask the radiated sinusoidal sound field as

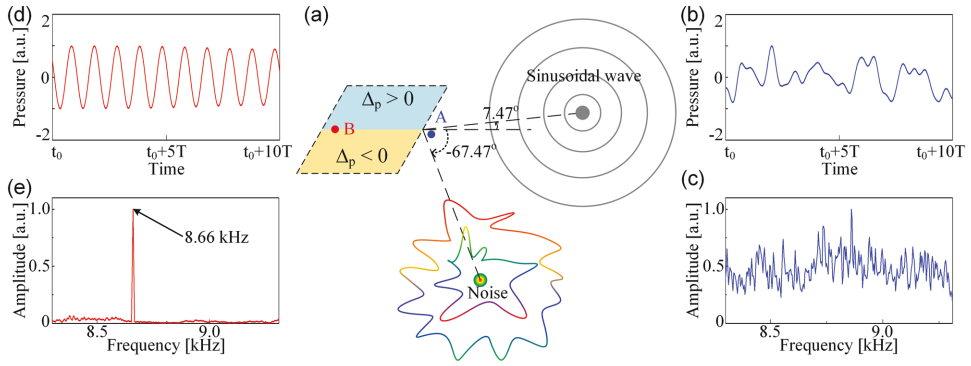

Figure 6. Demonstration of anti-interference acoustic communication with a TAA. a) Experimental schematics: a sound source of preference emits sinusoidal waves (gray solid circles) with frequency $f = 8.66$ kHz. The external interference source radiates broadband white noise (rainbow-colored solid curves) to mask the desired signal. b) Pressure signals in the time-domain and c) corresponding FFT spectra of the signal measured at the near-side of the TAA (labeled as A in panel (a)). d,e) Same as (b) and (c) but measured at the antenna terminal (labeled as B in panel (a)). $T = 1/f$ is the time period of sound wave.

emitted from a point source that is located at 7.47° from the interface, by deliberately introducing extraneous broadband white noise (such as traffic or air condition noise), whose source is placed at −67.47°. Here we show how the TAA can pick up specific signals from a desired direction in a noisy acoustic environment. As illustrated in the schematics of Figure 6a we detect the signals at both ports of the antenna. The measured time-domain pressure at points *A* and *B*, shown in Figure 6b,d, respectively, illustrates how the emitted sinusoidal wave is corrupted by interfering noise but when detected by the TAA, the otherwise random signal regains its monochromatic sinusoidal shape. Consequently, the acoustic information perceived by the listener, thanks to the TAA, is obtained from a desired direction and free from any competing signals. As seen in Figure 6c,e, we measure the corresponding fast-Fourier-transform (FFT) spectra, in which the sound energy at point *A* is continuously distributed over the entire spectrum, while the sound energy content at point *B* features the only sharp peak at the desired signal frequency of $f = 8.66$ kHz. Here, the signal-interference-ratio, which can be determined by the energy ratio between the desired signal and the noise, has an increment of 27.6 dB. We emphasize that the sound sources in Figure 6 are located far enough away from the proposed TAA such that the wavefronts impinging on the array can be modeled as plane waves (the far-field assumption). Furthermore, we also investigate the special case where the signal and noise sources are located close to the TAA (the conventional far-field assumption is not valid). The results show that the TAA still discriminates between desired and unwanted signals irrespective of the physical locations from which they originate, confirming the immunity to various acoustic circumstances (Note S14, Supporting Information). Similarly, efficient anti-interference communication can also be realized by a TAA with a negative-type interface (Note S15, Supporting Information).

To sum up, theoretically and experimentally we proposed valley-Hall topological insulators acting efficiently as sound transmitting and receiving antennas. The approach was inspired by the biosonar of dolphins that can pick up specific signals from a desired direction in a noisy acoustic environment, which we mimicked with a Kagome lattice made of epoxy resin rods. Based on such platform, we have experimentally put forward a prototype topological acoustic antenna that is capable of out-coupling and sustaining valley-polarized edge states permitting energy efficient communication. The proposed duplex antenna not only supports superdirective needle-like sound radiation with less than a 10° beamwidth, but also achieves anti-interference sound reception in various acoustic environments while being immune to white noise. This topological acoustic antenna provides the unique possibility to advance communication technologies such as hands-free smartphones and noise-immune hearing aids, but also to improve sonar applications with highly directional collimated beams and underwater communications at efficient energy levels.

Experimental Section

The rods of TAA were precision-fabricated using epoxy resin via 3D printing. The fabricated TAA sample in Figure 3b consisted of 2700 rods embedded in an air matrix. The height of the rods, which were placed between two parallel plates of Plexiglass, was chosen to be 1.40 cm. In this scenario, the 2D approximation is applicable since the planar waveguide supports propagating mode uniformly along the rod-axis for the wavelengths under consideration. Experiments were conducted by two identical loudspeakers (ENPILL PD-2121) with graded pipes to generate a point sound source. Cone-shaped sound absorbing foams were mounted around the testing area to minimize the boundary reflections by the open space. Local pressure fields were measured by inserting 1/4 in. condensed microphones (GRAS type 40PH) into the top plate at the designated positions. The outputs of the microphones were acquired by a digitizer (NI PXI-4498), and processed by LabVIEW software. A frequency scan was performed from 8.30 to 9.31 kHz with an increment of 0.01 kHz. To show the far-field radiative directivity of the topological acoustic antenna, the distance between the exit of the topological waveguide and the measuring microphones was chosen to be $D = 0.651$ m. An angular scan was performed from −120° to 60° with an increment of 3°. Highly reliable readings of pressure amplitude at each frequency were ensured by multiple measurements, from which the complex transmission/sound intensity was obtained by means of the transfer matrix method.

Supporting Information

Supporting Information is available from the Wiley Online Library or from the author.

Acknowledgements

Z.Z. and Y.T. contributed equally to this work. This work was supported by National Key R&D Program of China (2017YFA0303702), NSFC (11674172, 11574148, and 11474162), Jiangsu Provincial NSF (BK20160018), the Fundamental Research Funds for the Central Universities (020414380001) and Nanjing University Innovation and Creative Program for Ph.D. candidate (CXCY17-11). J.C. acknowledges the support from the European Research Council (ERC) through the Starting Grant 714577 PHONOMETA and from the MINECO through a Ramón y Cajal grant (Grant No. RYC-2015-17156).

Conflict of Interest

The authors declare no conflict of interest.

Keywords

acoustic antennas, superdirectivity, topological edge states, valley-Hall phase

Received: May 21, 2018
Revised: June 20, 2018
Published online: July 30, 2018

[1] W. A. Yost, G. Gourevitch, *Directional Hearing*, Springer-Verlag, New York **1987**.
[2] W. W. L. Au, *The Sonar of Dolphins*, Springer-Verlag, New York **1993**.
[3] Y. Zhang, Z. Song, X. Wang, W. Cao, W. W. L. Au, *Phys. Rev. Appl.* **2017**, *8*, 064002.
[4] M. B. D. Ward, *Microphone Arrays Signal Processing Techniques and Applications*, Springer-Verlag, Berlin **2001**.
[5] M. Ke, Z. Liu, P. Pang, C. Qiu, D. Zhao, S. Peng, J. Shi, W. Wen, *Appl. Phys. Lett.* **2007**, *90*, 083509.
[6] G. Lu, E. Ding, Y. Wang, X. Peng, J. Cui, X. Liu, X. Liu, *Appl. Phys. Lett.* **2017**, *110*, 123507.
[7] J. Christensen, A. I. Fernandez-Dominguez, F. de Leon-Perez, L. Martin-Moreno, F. J. Garcia-Vidal, *Nat. Phys.* **2007**, *3*, 851.
[8] Y. Cheng, J. Y. Xu, X. J. Liu, *Appl. Phys. Lett.* **2010**, *96*, 071910.
[9] J.-W. Wang, Y. Cheng, X.-J. Liu, *Chin. Phys. B* **2014**, *23*, 054301.
[10] B.-G. Yuan, Y. Cheng, X.-J. Liu, *Appl. Phys. Express* **2015**, *8*, 027301.
[11] Z. Yang, F. Gao, X. Shi, X. Lin, Z. Gao, Y. Chong, B. Zhang, *Phys. Rev. Lett.* **2015**, *114*, 114301.
[12] V. Peano, C. Brendel, M. Schmidt, F. Marquardt, *Phys. Rev. X* **2015**, *5*, 031011.
[13] M. Xiao, W.-J. Chen, W.-Y. He, C. T. Chan, *Nat. Phys.* **2015**, *11*, 920.
[14] A. B. Khanikaev, R. Fleury, S. H. Mousavi, A. Alu, *Nat. Commun.* **2015**, *6*, 8260.
[15] Z.-G. Chen, Y. Wu, *Phys. Rev. Appl.* **2016**, *5*, 054021.
[16] R. Fleury, A. B. Khanikaev, A. Alu, *Nat. Commun.* **2016**, *7*, 11744.
[17] C. He, X. Ni, H. Ge, X.-C. Sun, Y.-B. Chen, M.-H. Lu, X.-P. Liu, Y.-F. Chen, *Nat. Phys.* **2016**, *12*, 1124.
[18] J. Mei, Z. Chen, Y. Wu, *Sci. Rep.* **2016**, *6*, 32752.
[19] C. He, Z. Li, X. Ni, X.-C. Sun, S.-Y. Yu, M.-H. Lu, X.-P. Liu, Y.-F. Chen, *Appl. Phys. Lett.* **2016**, *108*, 031904.
[20] Y.-G. Peng, C.-Z. Qin, D.-G. Zhao, Y.-X. Shen, X.-Y. Xu, M. Bao, H. Jia, X.-F. Zhu, *Nat. Commun.* **2016**, *7*, 13368.
[21] Z. Yang, B. Zhang, *Phys. Rev. Lett.* **2016**, *117*, 224301.
[22] Z. Zhang, Q. Wei, Y. Cheng, T. Zhang, D. Wu, X. Liu, *Phys. Rev. Lett.* **2017**, *118*, 084303.
[23] Q. Wei, Y. Tian, S. Y. Zuo, Y. Cheng, X. J. Liu, *Phys. Rev. B* **2017**, *95*, 094305.
[24] J. Lu, C. Qiu, L. Ye, X. Fan, M. Ke, F. Zhang, Z. Liu, *Nat. Phys.* **2017**, *13*, 369.
[25] C. Brendel, V. Peano, O. J. Painter, F. Marquardt, *Proc. Natl. Acad. Sci. USA* **2017**, *114*, E3390.
[26] N. Xiang, A. G. Maxim, A. Andrea, B. K. Alexander, *New J. Phys.* **2017**, *19*, 055002.
[27] S. Yves, R. Fleury, T. Berthelot, M. Fink, F. Lemoult, G. Lerosey, *Nat. Commun.* **2017**, *8*, 16023.
[28] B.-Z. Xia, T.-T. Liu, G.-L. Huang, H.-Q. Dai, J.-R. Jiao, X.-G. Zang, D.-J. Yu, S.-J. Zheng, J. Liu, *Phys. Rev. B* **2017**, *96*, 094106.
[29] Z. Zhang, Y. Tian, Y. Cheng, X. Liu, J. Christensen, *Phys. Rev. B* **2017**, *96*, 241306.
[30] B.-Z. Xia, S.-J. Zheng, T.-T. Liu, J.-R. Jiao, N. Chen, H.-Q. Dai, D.-J. Yu, J. Liu, *Phys. Rev. B* **2018**, *97*, 155124.
[31] J. Lu, C. Qiu, W. Deng, X. Huang, F. Li, F. Zhang, S. Chen, Z. Liu, *Phys. Rev. Lett.* **2018**, *120*, 116802.
[32] F. Li, X. Huang, J. Lu, J. Ma, Z. Liu, *Nat. Phys.* **2018**, *14*, 30.
[33] Z. Zhang, Y. Tian, Y. Cheng, Q. Wei, X. Liu, J. Christensen, *Phys. Rev. Appl.* **2018**, *9*, 034032.
[34] D. Hsieh, D. Qian, L. Wray, Y. Xia, Y. S. Hor, R. J. Cava, M. Z. Hasan, *Nature* **2008**, *452*, 970.
[35] Z. Qiao, J. Jung, Q. Niu, A. H. MacDonald, *Nano Lett.* **2011**, *11*, 3453.
[36] J. Lu, C. Qiu, M. Ke, Z. Liu, *Phys. Rev. Lett.* **2016**, *116*, 093901.
[37] P. Raj Kumar, R. Massimo, *New J. Phys.* **2017**, *19*, 025001.
[38] X. Wu, Y. Meng, J. Tian, Y. Huang, H. Xiang, D. Han, W. Wen, *Nat. Commun.* **2017**, *8*, 1304.
[39] F. Zhang, A. H. MacDonald, E. J. Mele, *Proc. Natl. Acad. Sci. USA* **2013**, *110*, 10546.
[40] M. Ezawa, *Phys. Lett. A* **2014**, *378*, 1180.
[41] M. Tzuhsuan, S. Gennady, *New J. Phys.* **2016**, *18*, 025012.